Analysis of periodic patterns, noise characteristics, and predictive modeling of polar motion and length of day

Shirafkan, Shayan; Sharifi, Mohammad Ali; Belda, Santiago; Khazraei, Seyed Mohsen; Amiri-Simkooei, Alireza; Modiri, Sadegh

DOI
10.1016/j.asr.2025.05.090

Publication date
2025

Document Version
Final published version

Published in
Advances in Space Research

Citation (APA)
Shirafkan, S., Sharifi, M. A., Belda, S., Khazraei, S. M., Amiri-Simkooei, A., & Modiri, S. (2025). Analysis of periodic patterns, noise characteristics, and predictive modeling of polar motion and length of day. *Advances in Space Research*, *76*(5), 2594-2607. https://doi.org/10.1016/j.asr.2025.05.090

Available online at www.sciencedirect.com

ScienceDirect

Advances in Space Research 76 (2025) 2594–2607

ADVANCES IN SPACE RESEARCH (a COSPAR publication)

www.elsevier.com/locate/asr

Analysis of periodic patterns, noise characteristics, and predictive modeling of polar motion and length of day

Shayan Shirafkan [a], Mohammad Ali Sharifi [a,*], Santiago Belda [b], Seyed Mohsen Khazraei [c], Alireza Amiri-Simkooei [d], Sadegh Modiri [e]

[a] School of Surveying and Geospatial Engineering, College of Engineering, University of Tehran, Tehran, Iran
[b] UAVAC, Department of Applied Mathematics, Universidad de Alicante, Alicante, Spain
[c] Department of Surveying Engineering, Faculty of Civil Engineering, Jundi-Shapur University of Technology, Dezful, Iran
[d] Faculty of Aerospace Engineering, Delft University of Technology, Delft, the Netherlands
[e] Federal Agency for Cartography and Geodesy (BKG), Frankfurt am Main, Germany

Received 31 January 2025; received in revised form 13 May 2025; accepted 30 May 2025
Available online 6 June 2025

Abstract

Earth orientation parameters (EOP) are critical for applications in orbit determination, astronomy, space geodesy, and geophysics. Accurate predictions of EOP rely on the identification of both deterministic periodic patterns and noise characteristics. This study addresses these requirements by analyzing the Polar Motion (PM) and Length Of Day (LOD) time series to determine its stochastic model structure, estimated using least squares variance component estimation (LS-VCE). With this model, deterministic periodic patterns were extracted through least squares harmonic estimation (LS-HE) and validated against colored noise components to identify significant signals. Using the IERS 14 C04 data from January 1, 2000, to December 31, 2019, the study identified the noise as power-law with a spectral index of −1.5, suggesting non-stationary fractional Brownian characteristics. LS-HE detected dominant frequencies in PM–notably the Chandler and annual signals–and in LOD, with annual, semiannual, 14-day, and 9-day signals. Building on these findings, short-, mid-, and long-term prediction model were developed for the PM and LOD time series from September 2021 to December 2022. The predictive model combines the LS-HE-extracted signals and the noise model to generate forecasts. These predictions were compared with other models from the Second Earth Orientation Parameter Prediction Comparison Campaign, demonstrating competitive accuracy, particularly for the initial forecast days. The results validate that combining LS-HE with a realistic noise model provides an effective approach for short-term of the PM and LOD forecasting, meeting the accuracy goals of geodetic and geophysical applications.

Keywords: EOP; LS-HE; VCE; Noise model

1. Introduction

The Earth undergoes continuous rotation about its axis, influenced by both internal and external processes. Understanding variations in this rotation is essential for a range of scientific and applied disciplines, including geophysics, astronomy, and space geodesy. Earth Orientation Parameters (EOP) represent five angles (x, y, UT1-UTC, dX, and dY) that define Earth's orientation in space, providing a critical link between terrestrial and celestial reference frames. Polar Motion (PM), described by the x and y coordinates of the celestial intermediate pole (CIP) relative to

* Corresponding author.
E-mail addresses: sharifi@ut.ac.ir (M.A. Sharifi), sharifi@ut.ac.ir (S. Modiri).

https://doi.org/10.1016/j.asr.2025.05.090

the terrestrial reference frame, captures changes in Earth's orientation due to mass redistribution and dynamic processes. Earth's rotation angle is represented by UT1-UTC ($\Delta UT1$), while changes in rotation rate, or Length of Day (LOD), reflect variability in Earth's rotational velocity (Tapley et al., 1985; Lichten et al., 1992; Schuh and Schmitz-Hübsch, 2000). Additionally, Celestial Pole Motion (CPM), characterized by deviations of the celestial pole from its conventional location via dX and dY offsets, further informs Earth's dynamic orientation (Belda et al., 2018; Mathews et al., 2002). High-precision EOP data are obtained from space geodetic methods such as very long baseline interferometry (VLBI), satellite laser ranging (SLR), and global navigation satellite systems (GNSS). VLBI uniquely provides access to all EOP components, yet real-time EOP data availability is limited by processing complexity, underscoring the need for reliable predictive methods (Stamatakos, 2017; Modiri et al., 2024).

Analyzing EOP provides insights into Earth's fluid dynamics on a global scale, meeting critical research needs across geophysics, meteorology, oceanography, geomagnetism, and hydrology (Guinot et al., 1980). Key influencing factors, such as sea level changes, atmospheric and oceanic mass redistribution, tidal deformation, and angular momentum exchange, significantly affect PM and Earth's rotation (Rochester et al., 1984). In recent years, research has advanced our understanding of the geophysical drivers of PM, highlighting influences from processes such as glacial isostatic adjustment, mantle convection, and climate-induced mass redistribution Ray and Erofeeva (2014); Bizouard et al. (2022). Previous studies have documented seasonal patterns in EOP. For example, PM time series are dominated by the Chandler wobble (approximately 14 months), an annual signal, and additional semiannual and quarterly variations. Similarly, LOD exhibits annual, semiannual, and shorter periodic fluctuations (Iz, 2008; Shen and Peng, 2016). Temporal variations in these periodic amplitudes suggest complex excitation mechanisms, including atmospheric and oceanic interactions (Chen and Wilson, 2005; Michalczak et al., 2024).

The stochastic characteristics of EOP time series–particularly those associated with long-memory colored noise–remain less investigated. In a previous study on PM time series noise addressed by (Bizouard, 2020), given n solutions pertaining to the pole coordinates derived from a specified methodology throughout the temporal intervals (2000–2019 for GNSS, 2004–2019 for SLR, and 1990–2019 for VLBI), Bizouard constructed $n(n–1)/2$ paired differences. Systematic inaccuracies at a designated period or frequency are identified through the discrete Fourier spectrum, while the stochastic uncertainty can be evaluated by examining the Allan deviation. The findings were articulated with respect to GNSS time series. Bizouard presents a frequency modulation flicker noise or a pink noise characterized by power spectral density and spectral amplitude, respectively. Subsequently, this study selected three SLR solutions. The Allan deviation of the corresponding paired differences exhibited slopes ranging from 0 to 1.3 commencing from a duration of 10 days, with a noise magnitude at least twice that observed for GNSS. Following the SLR analysis, they selected five VLBI series over time spans ranging from 10 days to inter-annual periods. The Allan deviations of the corresponding paired differences displayed slopes approaching 1.2 on a log–log scale.

In addition, stochastic models, including autoregressive (AR), autoregressive moving average (ARMA), and autoregressive integrated moving average (ARIMA) models, are commonly employed to capture temporal correlations in time series data. In these models, the AR component reflects the influence of past values, the moving average (MA) component accounts for past errors, and the integrated component in ARIMA enables differencing to stabilize non-stationary series. While these models effectively capture certain types of temporal correlation, they may fall short of fully characterizing the complex noise properties inherent to EOP time series. A deeper understanding of these noise characteristics could substantially enhance prediction accuracy and reliability (Hamdan and Sung, 1996; Iz, 2008; Guo et al., 2013; Shen et al., 2018; Wu et al., 2021; Jin et al., 2021b). Recently, methods that incorporate derivative information into PM predictions have demonstrated improved stability and accuracy in short-term forecasts by integrating derivative components specific to EOP dynamics (Michalczak et al., 2024).

There is a substantial body of literature dedicated to studying the prediction of PM and LOD, which warrants further analysis and summarization. Various approaches have been explored: Single Mathematical Method, Combined Mathematical and Physical Methods, and Integrated Mathematical Methods. AR Models (Kosek et al., 1998), Least Squares (LS) collocation (Włodzimierz, 1990), artificial neural network (ANN) (Schuh et al., 2002; Kalarus and Kosek, 2004) are some examples of Single Mathematical Method to predict PM and LOD. Combination of the methods that take into account the axial component of effective angular momentum (Freedman et al., 1994; Gross et al., 1998; Johnson et al., 2005; Niedzielski and Kosek, 2008; Nastula et al., 2012; Dill et al., 2019; Modiri et al., 2020) are some examples of Combined Mathematical and Physical Methods. Some studies, like (Zotov et al., 2018), have integrated multiple predictive approaches with Astronomical Observations. In addition, Machine Learning (ML) approaches (Wang and Zhang, 2023; Kiani Shahvandi et al., 2022; Kur et al., 2024; Dhar et al., 2024), including physics-informed neural networks (PINNs), have incorporated these geophysical constraints to enhance predictive accuracy (Kiani Shahvandi et al., 2024). Identifying both deterministic periodic patterns and stochastic characteristics in EOP is thus crucial for refining prediction models and enabling high-precision applications. Therefore, the hybrid methods can effectively be used to the prediction of EOP. Prediction methods span from classical LS extrapolation and AR models (Kosek et al., 1998; Kosek et al., 2007; Xu et al., 2012) to advanced ML models that

effectively capture the complex patterns in EOP time series, particularly in short-term forecasting (Guessoum et al., 2022; Dhar et al., 2024). In addition, combination of the Singular Spectrum Analysis (SSA) with ARMA, Copula, or Multilayer Perceptron (MLP) (Modiri et al., 2018; Shen et al., 2018; Jin et al., 2021b; Jin et al., 2021a; Kong et al., 2023; Wu et al., 2023) are some example of the Integrated Mathematical Methods. For example, in the studies applied by Jin et al. (2021a) the MLP is introduced into PM prediction. They try for the first time to combine MLP with ARMA and SSA for the mid- and long-term prediction of PM. The principal components of PM were extracted and predicted by SSA first. Then, the combined MLP and ARMA were used to predict the residual term. In addition, Wu et al. (2023) combined MLP, SSA and ARMA for short- and long-term PM prediction. MLP was introduced into PM prediction due to its automatic learning characteristics and its ability to effectively process nonlinear and multi-dimensional data. The SSA was used to extract and predict the principal components of PM, while the remaining components were predicted using ARMA. In the meantime, SSA and ARMA were used to provide training data and target learning data for the MLP model.

The International Earth Rotation and Reference Systems Service (IERS) has led two Earth Orientation Parameter Prediction Comparison Campaigns (EOP PCC) to assess prediction methods. Findings from the first campaign (2005–2009) suggested that no single approach is optimal across all EOP components and prediction intervals, promoting the development of hybrid prediction models (Kalarus et al., 2010). The ongoing second campaign (since 2021) has emphasized advancing predictive techniques, including machine learning and statistical innovations, such as vector autoregressive (VAR) models, which model residual processes jointly with primary time series (Sliwinska-Bronowicz et al., 2024; Michalczak et al., 2024).

Given the critical role of the PM and LOD in numerous applications, this study addresses the following research questions: i) How can the deterministic periodic patterns and noise characteristics of the PM and LOD can be effectively modeled and quantified to enhance short-term prediction accuracy? ii) What are the dominant frequencies within the PM and LOD time series, and how do they contribute to overall behavior and predictability? iii) How effective is a hybrid model that integrates periodic and noise components in improving prediction reliability for real-time applications? To address these questions, we hypothesize that the PM and LOD time series exhibit a power-law (PL) noise process, similar to many geophysical phenomena (Mandelbrot, 1982; Agnew, 1992; Williams, 2003; Williams et al., 2004; Amiri-Simkooei, 2007). By isolating colored noise from true periodic signals, we aim to establish a robust functional and stochastic model for PM and LOD, estimated through least squares variance component estimation (LS-VCE) and least squares harmonic estimation (LS-HE). Our objective is to enhance the precision of the PM and LOD predictions for real-time applications in disciplines that depend on accurate Earth orientation data.

This paper is structured as follows: Section 2 discusses the noise characteristics of the PM and LOD time series. Section 3 examines deterministic the PM and LOD patterns. Section 4 details LS-HE frequency extraction. Section 5 presents a short-term the PM and LOD forecast and compares it to benchmarks from the second EOP PCC. Finally, Section 6 summarizes findings and concludes the study.

2. Noise characteristics of the PM and LOD time series

Similar to many geophysical time series, it is expected that the error sources in the PM and LOD observations introduce temporal correlations into the time series (Agnew, 1992). Accordingly, the frequency-domain behavior of the PM and LOD time series as a stochastic process can be described as a power law (PL) process. In a PL process, the power spectrum is proportional to the κ^{th} power of temporal frequency f (Mandelbrot, 1982; Agnew, 1992; Williams, 2003; Williams et al., 2004; Amiri-Simkooei, 2007). The spectral index κ usually ranges between $-3 < \kappa < 1$. A negative spectral index indicates more noise power at low frequencies. Among various spectral indices, $\kappa = 0, \kappa = -1$, and $\kappa = -2$ are commonly referred to as well-known power-law noises, representing white noise, flicker noise, and nonstationary random walk noise, respectively. Spectral indices $-1 < \kappa < 1$ confirm the stationarity of the time series.

The stochastic behavior of an m-dimensional power law process with spectral index κ can also be described by a PL noise covariance matrix Q_{PL} (Bos et al., 2008):

$$Q_{PL} = \Delta T^{\frac{-\kappa}{2}} U^T U \tag{1}$$

where

$$U = \begin{bmatrix} h_0 & h_1 & \cdots & h_N \\ 0 & h_0 & \cdots & h_{N-1} \\ \vdots & \vdots & \ddots & \vdots \\ 0 & 0 & \cdots & h_0 \end{bmatrix} \tag{2}$$

and

$$h_i = \frac{\frac{-\kappa}{2} + i - 1}{i} h_{i-1}, \quad h_0 = 1 \tag{3}$$

where ΔT is the sampling rate, considered to be $\Delta T = \frac{1}{365.25}$ years for daily geodetic time series.

2.1. Stochastic model identification

For a time series of m observations $\mathbf{y} = [y_1 \quad y_2 \quad \cdots \quad y_m]^T$, considering the total noise as a combination of pure white noise with variance σ_w^2 and PL noise with variance

σ_{PL}^2, the covariance matrix Q of observations can be modeled as

$$D(\mathbf{y}) = Q = \sigma_w^2 Q_w + \sigma_{PL}^2 Q_{PL} \tag{4}$$

which represents the stochastic model of the PM and LOD time series. This stochastic model can be formulated individually for the time series of the x and y coordinates of the pole (PM) and LOD, assuming they are uncorrelated in pairs. Also, Q_w is a matrix with size $m \times m$ and is defined by the following equation:

$$Q_w = \mathrm{diag}(\sigma_1^2, \sigma_2^2, \ldots, \sigma_m^2) \tag{5}$$

where diag is the operator of matrix diagonalization and σ_i^2's are the precision of the observations. In other words, in the above matrix, these precisions play the role of weight because older the PM and LOD observations always have less accuracy than newer observations. Eq. (5) produces a cofactor matrix corresponding to a non-stationary white noise model. When considering the two coordinate components of PM to be correlated, the same noise structure (PL noise) is expected for both components. The multivariate stochastic model can then be formulated for the PM time series $\mathbf{y_1}$ and $\mathbf{y_2}$ (time series of the x and y coordinates of the pole, respectively) as follows:

$$D(\mathrm{vec}(\mathbf{Y})) = \Sigma \otimes Q \tag{6}$$

where vec and $\otimes$ are the vectorization and Kronecker product operators, respectively, $\mathbf{Y} = [\mathbf{y_1} \quad \mathbf{y_2}]$ is the observation matrix, $\Sigma = \begin{bmatrix} \sigma_1^2 & \sigma_{12} \\ \sigma_{12} & \sigma_2^2 \end{bmatrix}$ describes the between-series correlation with the (co) variances $\sigma_{ij}, i, j = 1, 2$, and Q represents the time correlation in the time series, similar to Eq. (4). Because the two components of PM share the same structure, they are examined using a multivariate framework. As a result, the correlation between PM x and PM y is represented in the covariance matrix Σ and is assessed through the multivariate LS-VCE (Amiri-Simkooei, 2007). In contrast, the LOD time series presents a more intricate structure.

The stochastic model identification of the PM and LOD time series can be conducted in two steps. First, the PL spectral index κ needs to be determined. This can be achieved through methods such as the w-test and Log-likelihood statistics (Amiri-Simkooei, 2007), or by estimating the slope of the power spectra in log–log space (Nikolaidis, 2002). Due to the non-stationary behavior of the PM and LOD time series and variations in periodic patterns that are not fully modeled by the trigonometric terms of the functional model, the slope estimation method in log–log space provides a more reliable estimate of the spectral index. In this study, the univariate and multivariate least squares harmonic estimation (LS-HE) power spectrum is used for this purpose (see Section 3.1). Second, the unknown parameters of the stochastic model need to be estimated. The unknown variances σ_w^2 and σ_{PL}^2 in Eq. (4) and the between-series (co) variances $\sigma_{ij}, i, j = 1, 2$, can be estimated using the univariate or multivariate LS-VCE.

2.2. Least squares variance component estimation (LS-VCE)

2.2.1. Univariate LS-VCE

Considering the deterministic behaviors to be modeled in a linear model of observation equations,

$$E(\mathbf{y}) = A\mathbf{x} \tag{7}$$

where E is the expectation operator, and A and $\mathbf{x}$ are the design matrix and unknowns of the functional model, respectively, the least squares estimate of the unknown variance components in the stochastic model of Eq. (4), $\mathbf{s} = [s_1 \quad s_2]^T = [\sigma_w^2 \quad \sigma_{PL}^2]^T$, can be obtained through

$$\hat{\mathbf{s}} = N^{-1}\mathbf{l} \tag{8}$$

where the entries of the normal matrix N and the vector $\mathbf{l}$ are

$$n_{kl} = \frac{1}{2}\mathrm{tr}(Q^{-1}P_A^{\perp}Q_kQ^{-1}P_A^{\perp}Q_l) \tag{9}$$

and

$$l_k = \frac{1}{2}\hat{\mathbf{e}}^T Q^{-1} Q_k Q^{-1} \hat{\mathbf{e}} \tag{10}$$

In the above equations, $k, l = 1, 2, Q_1 = Q_w$ and $Q_2 = Q_{PL}$ are the white and PL noise covariance matrices from Eq. (1), tr is the trace operator, and $\hat{\mathbf{e}} = P_A^{\perp}\mathbf{y}$ with $P_A^{\perp} = I - A(A^TQ^{-1}A)^{-1}A^TQ^{-1}$ as an orthogonal projector. Since Q appears in Eqs. (9) and (10), the variance components $\mathbf{s}$ are estimated iteratively, as discussed by Amiri-Simkooei et al. (2007, 2008).

2.2.2. Multivariate LS-VCE

We now formulate the multivariate functional model for the PM time series $\mathbf{y_1}$ and $\mathbf{y_2}$ as

$$E(\mathrm{vec}(\mathbf{Y})) = (I_2 \otimes A)\mathrm{vec}(\mathbf{X}) \tag{11}$$

where I_2 is the 2-dimensional identity matrix, and $\mathbf{X} = [\mathbf{x_1} \quad \mathbf{x_2}]$ is the unknown matrix in the functional model. The unknowns in the stochastic model of Eq. (6) are estimated in two steps (Amiri-Simkooei, 2009). The variance components $\mathbf{s} = [s_1 \quad s_2]^T = [\sigma_w^2 \quad \sigma_{PL}^2]^T$ are first estimated using Eq. (8) by calculating the entries of N and $\mathbf{l}$ as

$$n_{kl} = \frac{r}{2}\mathrm{tr}(Q^{-1}P_A^{\perp}Q_kQ^{-1}P_A^{\perp}Q_l) \tag{12}$$

and

$$l_k = \frac{m-n}{2}\mathrm{tr}\left(\hat{\mathbf{E}}^TQ^{-1}Q_kQ^{-1}\hat{\mathbf{E}}\left(\hat{\mathbf{E}}^TQ^{-1}\hat{\mathbf{E}}\right)^{-1}\right) \tag{13}$$

where $\hat{\mathbf{E}} = P_A^{\perp}\mathbf{Y}$. The (co) variance matrix Σ is then estimated as

$$\hat{\Sigma} = \frac{\hat{\mathbf{E}}^T Q^{-1} \hat{\mathbf{E}}}{m-n} \tag{14}$$

3. Deterministic patterns of the PM and LOD time series

The deterministic variations in the PM and LOD time series can be effectively modeled using the Least Squares Harmonic Estimation (LS-HE) method. This approach formulates the time series within a robust functional model, typically including a linear trend component along with multiple periodic signals, which employed in many different time series. LS-HE is applicable in both univariate and multivariate forms (Amiri-Simkooei, 2007). For analyzing the PM represented by the x and y coordinates of the pole, a bivariate LS-HE routine provides an appropriate framework (Amiri-Simkooei, 2013).

3.1. LS-HE methodology

3.1.1. Univariate LS-HE

Consider a time series of m observations, $y = [y_1, y_2, \ldots, y_m]^T$, which consists of a linear trend and q seasonal signals with frequencies $\omega_k, k = 1, \ldots, q$. The functional model for this time series can be expressed as:

$$E(y) = Ax + \sum_{k=1}^{q} A_k x_k, \tag{15}$$

where

$$A = \begin{bmatrix} 1 & t_1 \\ 1 & t_2 \\ \vdots & \vdots \\ 1 & t_m \end{bmatrix}, \quad A_k = \begin{bmatrix} \cos(\omega_k t_1) & \sin(\omega_k t_1) \\ \cos(\omega_k t_2) & \sin(\omega_k t_2) \\ \vdots & \vdots \\ \cos(\omega_k t_m) & \sin(\omega_k t_m) \end{bmatrix}. \tag{16}$$

In this setup, the vector $x = [y_0, r]^T$ contains the linear regression parameters (intercept and slope), while the vectors $x_k = [a_k, b_k]^T$ hold the coefficients for the cosine and sine components of the seasonal signals, from which the phase and amplitude can be determined.

The primary objective of LS-HE is to identify the significant frequencies $\omega_k, k = 1, \ldots, q$, and to establish the number q of relevant periodic signals. LS-HE identifies these frequencies through a numerical procedure that evaluates the LS-HE power $P(\omega_j)$ for a discrete set of candidate frequencies $\omega_j, j = 1, 2, \ldots$, where:

$$P(\omega_j) = \hat{e}^T Q^{-1} A_j \left(A_j^T Q^{-1} P_A^{\perp} A_j \right)^{-1} A_j^T Q^{-1} \hat{e}, \tag{17}$$

with $\hat{e} = P_A^{\perp} y$ and $P_A^{\perp} = I - A\left(A^T Q^{-1} A\right)^{-1} A^T Q^{-1}$. Here, Q denotes the covariance matrix of observations, as introduced in Section 2.1. Frequencies are explored from the Nyquist frequency up to the total span of the time series, with progressively refined resolution. Peaks in the LS-HE power spectrum, corresponding to dominant frequencies ω_k, indicate statistically significant signals at a confidence level of $(1-\alpha)\%$ if $P(\omega_k) > \chi^2_\alpha(2,0)$ (Amiri-Simkooei, 2007).

3.1.2. Multivariate LS-HE

For paired m-length time series y_1 and y_2 sampled simultaneously (e.g., x and y coordinates of PM), the multivariate or bivariate functional model, in alignment with Eq. (15), is represented as:

$$E(\mathrm{vec}(Y)) = (I_2 \otimes A)\mathrm{vec}(X) + \sum_{k=1}^{q} (I_2 \otimes A_k)\mathrm{vec}(X_k), \tag{18}$$

where $Y = [y_1, y_2], X = [x_1, x_2]$, and $X_k = [x_{1k}, x_{2k}]$, with $k = 1, \ldots, q$, represent the matrices of time series observations, linear regression unknowns, and trigonometric unknowns, respectively. The LS-HE power spectrum for the multivariate case is given by:

$$P(\omega_j) = \mathrm{tr}\left(\hat{E}^T Q^{-1} A_j \left(A_j^T Q^{-1} P_A^{\perp} A_j \right)^{-1} A_j^T Q^{-1} \hat{E} \Sigma^{-1} \right), \tag{19}$$

where $\hat{E} = P_A^{\perp} Y$, and Σ and Q are derived through multivariate LS-VCE as discussed in Section 2.2. Identified signals appear as power spectrum peaks and are statistically significant if $P(\omega_k) > \chi^2_\alpha(4,0)$ (Amiri-Simkooei, 2013).

4. Results and discussion

The results and discussion are organized into four subsections, presenting the analysis of both stochastic and deterministic variations in the PM components (x and y) and the LOD time series. The widely used IERS EOP 14 C04 data, which is available since January 1, 1962 Bizouard et al. (2019), was utilized in this study. For brevity, we refer to the IERS EOP 14 C04 time series as PM time series, LOD time series, or collectively as EOP time series. Before processing, periodic corrections were applied based on the 2010 IERS conventions (Petit and Luzum, 2010). These corrections account for tidal rigidity and oceanic tidal effects in the LOD time series, which were removed to yield the corrected LOD series, termed LODR. Fig. 1 displays the LOD time series with and without these effects. The time series span from January 1, 1998 to December 31, 2019, with a length of 24 years.

To evaluate the accuracy of this modeling in representing solid Earth and ocean tides in the LOD time series, we analyzed the amplitude of these signals in the LOD time series, the solid Earth plus ocean tide modeling time series, and the LODR time series. Table 1 shows the amplitude sizes of some of these signals. According to this table, it is clear that there are still effects of tidal signals of land and ocean rigidity in the LODR time series. These effects should be detected by the LS-HE method in the next steps, as expected. The correlation between these three time series was also calculated to assess the accuracy of the tidal signal modeling. Table 2 shows the results.

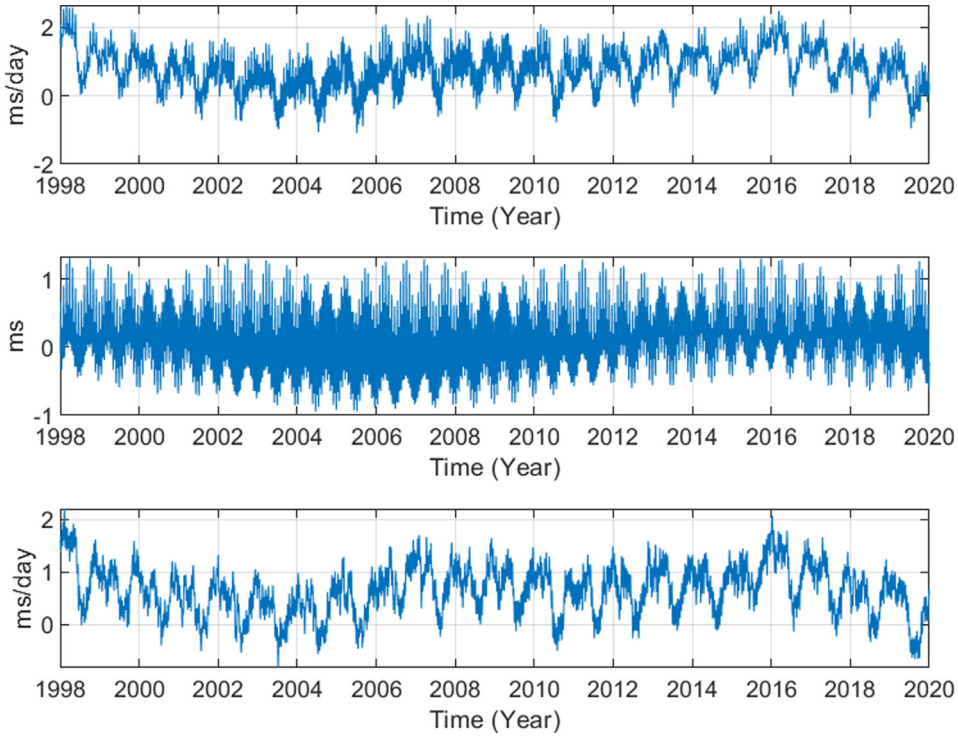

Fig. 1. LOD time series (top), the solid Earth plus ocean tide terms (middle), and the corrected LODR time series (bottom).

Table 1
The amplitude of some solid Earth tide signals in the LOD, the solid Earth plus ocean tide modeling, and LODR time series.

No.	Signal (days)	LOD (ms/day)	the solid Earth plus ocean tide (ms)	LODR (ms/day)
1	5.64	0.1163	0.1014	0.0125
2	9.54	0.1132	0.9584	0.0276
3	13.66	0.0513	0.0327	0.0157
4	27.44	0.0172	0.0094	0.0006

Table 2
The correlation between the solid Earth plus ocean tide time series with LOD, and LODR

Time series	LOD	LODR
The solid Earth plus ocean tide	0.5831	0.1207

4.1. Stochastic model identification

Similar to many geodetic time series, we consider the stochastic characteristics of the PM and LOD time series as a combination of pure white noise and PL noise with a spectral index of κ (Eq. 4). The optimal spectral index were determined using the LS-HE power spectra. The power spectra were calculated with the following three considerations. 1) the PM time series (x and y) were regarded as multivariate time series with identical characteristics. The multivariate and univariate LS-HE power spectra were thus calculated for PM and LOD series, respectively. 2) The power spectra were calculated considering white noise as the underlying noise (i.e., Q_w in Eqs. (17) and (19)). 3) Various power spectra were calculated for multiple windows of 10 year data. They were then averaged to obtain the smoothed spectrum for the PM and LOD series. This smoothing facilitates the observation of the power spectrum slope in the log–log space, and hence to identify the appropriate noise structure. The first window spanned from January 1, 1962 to December 31, 1973 and then they were slid forward by a two-year step. The last window spanned from January 1, 2008 to December 31, 2019, and therefore resulting in 24 power spectra.

The power spectra are illustrated in Fig. 2. The spectral values are plotted in log–log space against the period. The left frame shows the multivariate power spectrum of PM time series, and the right frame shows the LOD time series power spectrum. The spectra display distinct peaks that have corresponding underlying signals which we will explain later. However if we try to fit a line that can best approximate the power spectra (ignoring the seasonal signals), the one that goes through the power spectrum at high and low frequencies should be selected. It is observed, in

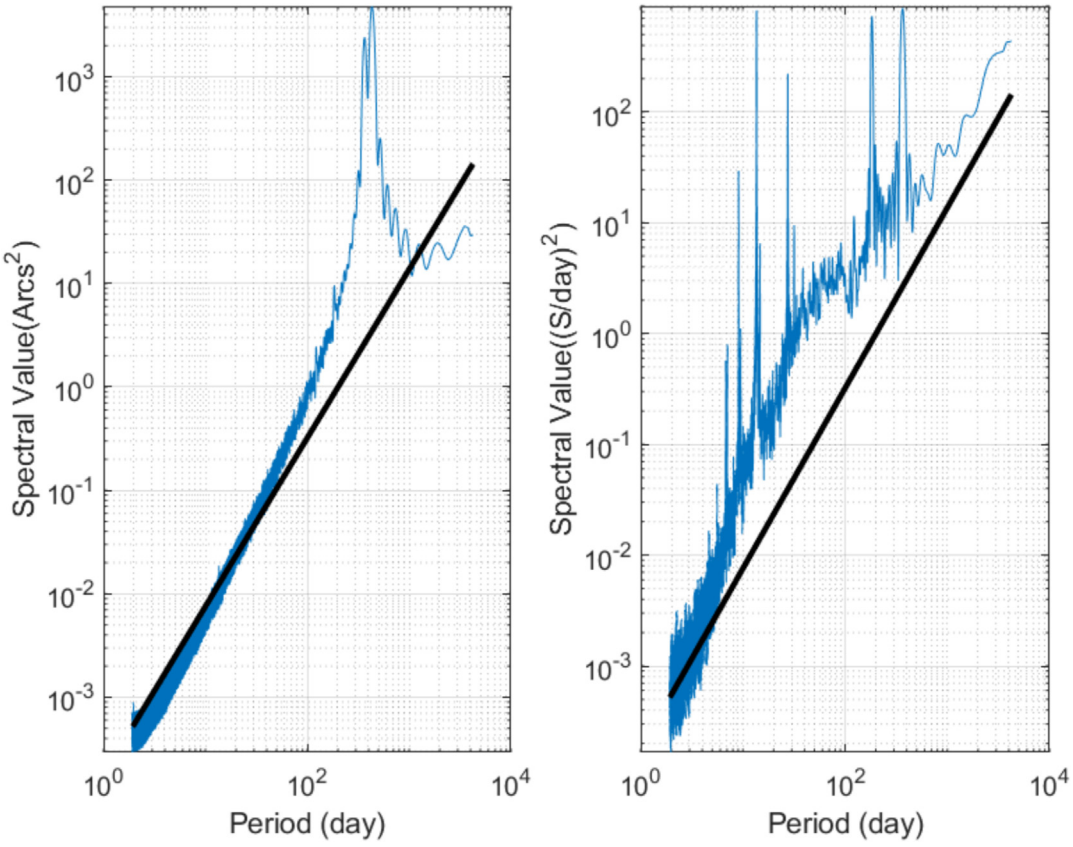

Fig. 2. Average power spectrum from 10-year windows for PM (left) and LOD time series (right), with log–log spectral values against the period. The best-fit line with a spectral index $\kappa = -1.5$ is shown in solid black.

both frames, that the line with the slope of 1.5 is best fitted (using least squares) to the power spectra. It is however noted that the 'linear fit' underestimates the spectral index at high frequency, but likely overestimates it at (very) low frequency, indicating that the spectral index is frequency dependent. This $\kappa = -1.5$ has also been confirmed when a line was fitted using the least squares method, excluding the peaks as being outliers in the fits. The PM and LOD time series are thus concluded to be optimally described with a combination of white noise and PL noise with a spectral index of$\kappa = -1.5$.

In a previous study conducted by (Bizouard, 2020), he obtained different slopes for each of the PM observations from different techniques. These slopes ranged from 0 to 1.3. Although the differences in methods cause differences in the results, it is noteworthy that in this study the processing was performed on the C04 time series of the PM and LOD, which is the result of combining different techniques. However, what both studies have in common is the presence of colored noise in the PM and LOD observations. This indicates that the noise in the PM and LOD time series is not stationary, especially at high and medium frequencies. This indicates that the long-term prediction can be a challenging task for this application. The above noise characteristics will be estimated and used for further analysis in this contribution.

4.2. Implementation of LS-HE

The LS-HE algorithm was applied to the PM and LOD time series in order to extract their periodic patterns. The 24-year data of the PM and LOD time series, from January 1, 1998 to December 31, 2019, where analyzed for this purpose. The multivariate and univariate LS-HE spectra were, once again, calculated for PM and LOD time series, considering the pre-identified structure of noise, with the PL spectral index $\kappa = -1.5$ in Eqs. (17) and (19)). The common signals were thus identified for the two components (x and y) of the PM time series. The extracted signals using LS-HE are listed in Table 3 with their amplitudes. The peaks in the LS-HE power spectra were evidence to find these signals. The statistical significance test will then be applied to test the validity of the detected signals (see Section 4.3).

In addition, as the time series are equally spaced, the Fast Fourier Transform (FFT) was applied to the time series to validate LS-HE results (Table 3). According to this table, the results of LS-HE and FFT are similar, with slight differences arising from the inherent characteristics of each method. For example, LS-HE allows analysis at user-specified frequencies, whereas FFT is limited to a fixed set of frequencies when computing the power spectrum.

Table 3
Extracted signals from the PM and LOD time series using LS-HE and FFT with unit days. The signals are manually identified from spectral peaks.

	PM Time Series (x and y)				LODR Time Series		
No.	LS-HE	FFT	x Amplitude (mas)	y Amplitude (mas)	LS-HE	FFT	Amplitude (ms/day)
1	433.61	433.60	79.74	79.82	364.63	365.25	0.32
2	366.51	365.25	112.43	102.43	182.72	182.50	0.22
3	231.91	233.50	2.92	15.75	121.81	121.75	0.04
4	183.62	183.50	2.81	20.37	27.51	27.60	0.03
5	123.91	121.75	1.07	6.23	13.66	13.60	0.21
6	13.66	13.60	0.12	3.82	9.13	9.20	0.04

In addition to these primary signals, high-frequency variations in the LODR series were observed. Additionally, some of these frequencies have well-established geophysical causes. Table 4 outlines the cause for the extracted frequencies. For example, in PM time series, the annual frequency is due to seasonal air and water mass redistributions and the Chandler frequency is due to the ocean-bottom pressure changes and fluctuations in the atmospheric pressure. In LODR time series, the causes for annual and semi-annual frequency are solar tides and ocean currents. It is important to note that the LS-HE does not account for changes in amplitude and phase, which likely contributes to discrepancies between the extracted signals and their nominal values. For instance, the deviation of the detected period from the tropical year's period is largely due to limitations in the analysis and methodology, such as the length of the time series, the sampling frequency used in spectrum calculations, or the difficulty in distinguishing between closely spaced frequencies. Regarding the Chandler wobble amplitude, this value has been decreasing over time. However, in the presented methodology, as with most parametric methods, signal amplitudes are assumed to remain constant. This represents a limitation of the LS-HE approach compared to nonparametric methods. Future research could explore amplitude modulation using the modulated LS-HE technique (Amiri-Simkooei and Asgari, 2012).

According to Fig. 2, the Chandler Wobble (CW) and the Annual Wobble (AW) were both in the spotlight. The CW is an excited resonance of the Earth's rotation, but since the Earth is a viscous-elastic body, it would decay freely to a minimum energy state of rotation around the figure axis over a period of approximately 68 years without any excitation (Gross, 2000; Gross et al., 2003; Lambeck, 2005; Wang et al., 2016). Although CW has been studied for over a century, its excitability mechanism remains elusive (Lenhardt and Groten, 1985; King and Agnew, 1991; Höpfner, 2004; Malkin and Miller, 2010). Various hypotheses for CW excitation have been proposed, e.g. atmospheric and oceanic processes (Brzeziński et al., 2002), variations in surface and wind pressure (Wahr, 1988), groundwater pressures, snow cover changes, interactions between core and mantle, and earthquakes (Dahlen, 1971; Höpfner, 2004).

The hydrologic contributions to the AW were examined by (Chao and O'Connor, 1988), who discovered that when the rainfall and snow load contributions from satellite data are combined, the land water contribution is significantly lower. According to Kuehne and Wilson (1991) analysis of the groundwater contribution using their global model compelled by monthly mean precipitation estimates, its amplitude in the prograde AW is only roughly 10 percent of the atmospheric contribution. Changes in atmospheric angular momentum (AAM) are a major contributor to the Earth's AW, according to some authors who calculated the atmospheric excitation of the AW using meteorological data available at various time spans and the PM excitation function (Munk and Mohamed Hassan, 1961; Wilson and Haubrich, 1976; Wahr, 1988). Also, Zhong et al. (2003) used a coupled ocean–atmosphere general circulation model to investigate the contributions of atmospheric, hydrologic, and ocean currents to seasonal PM. The results

Table 4
Known geophysical causes for extracted frequencies in the PM and LOD

NO	Periods of PM (days)	Cause (Iz, 2008)	Periods of LOD (days)	Cause
1	366.50	Seasonal air and water mass redistributions	364.68	Solar tides and ocean currents (Rosen, 1993; Höpfner, 1996)
2	433.61	Ocean-bottom pressure changes, and fluctuations in atmospheric pressure	182.75	Solar tides and ocean currents (Shen and Peng, 2016)
3	183.66	Seasonal air and water mass redistributions	121.86	Dynamics of the atmosphere and the oceans (Rosen, 1993; Höpfner, 1996)
4	231.96	Lateral heterogeneities, bifurcation solution	27.55	Lunar tides (Wahr, 1988)
5	123.93	Dynamics of the atmosphere and the oceans	13.66	Lunar tides (Wahr, 1988)

validated the significance of hydrology as a source of the AW. In addition, Gross et al. (2003) found that the effects of winds and currents on exciting the annual wobble have nearly the same retrograde amplitude and a prograde amplitude that differs by about 30 percent. They also found that the effect of currents on exciting the annual wobble is roughly two-thirds of the effect of bottom pressure variations.

The spectrum of the LOD time series can be categorized into three distinct components: low-frequency harmonic oscillations, oscillations associated with zonal solar (6 and 12 months) and lunar (27.54 days and its harmonics) tidal forces, and irregular variations occurring over timescales ranging from a few days to several decades. The low-frequency variations are predominantly attributed to the exchange of angular momentum between Earth's mantle and core, as the atmosphere lacks a sufficiently large angular momentum sink to account for these changes (Hide, 1977). For lunar influences, tidal zonal contributions are expected at the lunar month period (27.54 days) and its harmonics (13.77, 9.18, ...). Similarly, the solar synodic rotation period (27.27 days) and its harmonics (13.63, 9.09, ...) are anticipated to be present in the spectrum. In addition to elastic responses, the effects of mantle anelasticity and dynamic ocean tides further modulate the LOD variations. These effects manifest across a range of periods, from the 18.6-year lunar nodal tide to shorter periods such as 365.25 days, 182.62 days, 27.55 days, 13.66 days, 9.13 days, and 4.7 days. This comprehensive framework highlights the complex interplay of geophysical processes influencing Earth's rotational dynamics (Mouël et al., 2019).

4.3. Statistical significance test of detected signals

Although Table 3 provides a comprehensive list, some signals may not be significant in terms of their contributions to the PM and LOD series. For example, while the Chandler and annual signals are known to be significant (PM), some others signals provided in this table cannot likely contribute much. Their contribution is expected to be masked behind the colored noise level of the series. Therefore, after identification of all hand-picked signals by LS-HE, their corresponding statistical tests are conducted to find the significant signals in the presence of colored noise.

Fig. 3 shows the LS-HE spectrum for the LOD time series, adjusted for realistic noise using a model of white and PL noise ($\kappa = -1.5$). It is observed that the slope of the power spectrum reduces significantly compared to the right frame of Fig. 2. This happens due to the proper consideration of the noise model (see (Amiri-Simkooei, 2013)). The amplitudes of white noise and PL noise components, estimated by LS-VCE, in each of the PM and LOD time series, are listed in Table 5. The non-negative LS-VCE is used here not to estimate negative variance components. The white noise variance component is estimated to be zero for the three time series, which is likely due to the high level

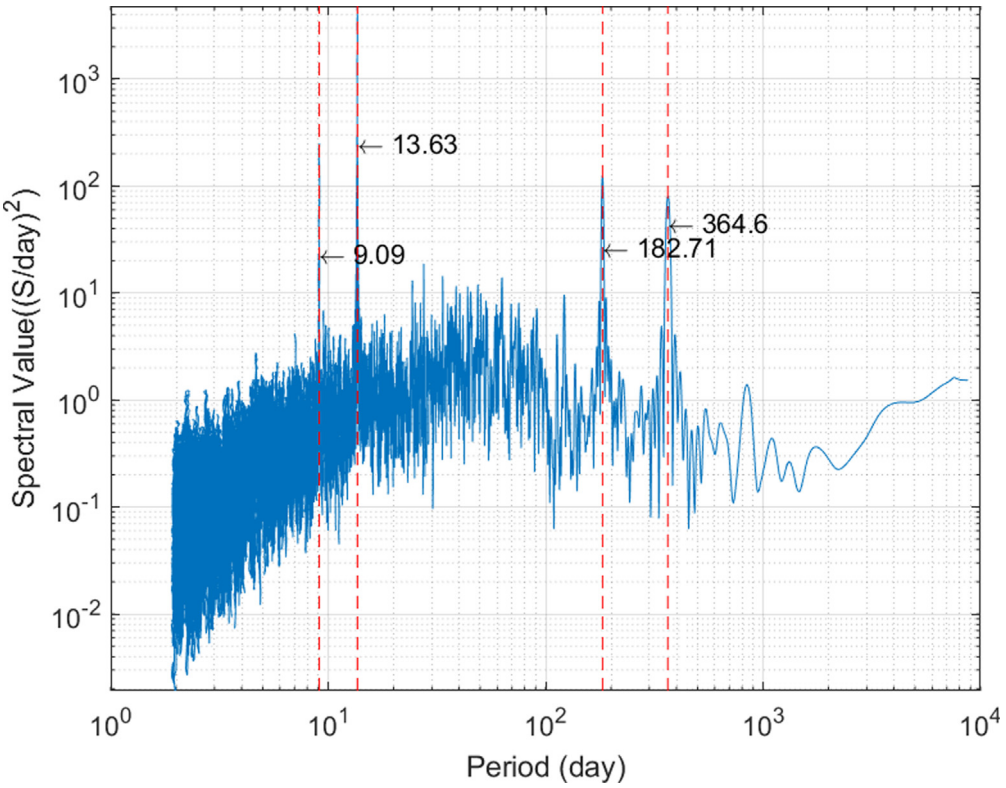

Fig. 3. Power spectrum of the LOD time series with a realistic noise model. Significant signals are marked by red dashed lines.

Table 5
Amplitude of noise components in the PM and LOD time series estimated using LS-VCE. The PL noise standard deviations are in mas/year$^{3/8}$ and (ms/day)/year$^{3/8}$ (see the structure of the power-law cofactor matrix in Eq. (1))

	PM Time Series (x and y)		
	x	y	LODR Time Series
White noise	0.002	0.001	0.0004
PL noise	18.29	17.16	0.82

Table 6
Significant periods (days) of the signals extracted from the PM and LOD time series using LS-HE.

LODR	PM (x and y)
364.68	433.61
182.75	366.50
13.66	–
9.13	–

of colored noise. For more information we refer to (Amiri-Simkooei, 2016). The functional model, used for estimating the variance components, is formed by a linear trend plus annual and Chandler signals for PM time series and linear trend plus annual and semi-annual signals for LODR (Xu et al., 2012). In the LS-VCE method, trends and harmonics are incorporated directly into the functional model. This is effectively equivalent to detrending the data and removing the signals from the time series. Comparing these noise amplitudes with the signal amplitudes presented in Table 3 it can be expected that some of the listed signals can be likely masked with colored noise. These signals are not recognized to be significant in the LS-HE statistical tests. Accordingly, the list of the identified signals would be much shorter. Table 6 presents the significant signals extracted from LS-HE. According to this table, the 433.61 (Chandler), and 366.50 (annual) days signals were identified as the significant signals in the PM time series. The deviation of the detected annual period (366.5 days) from the tropical year (365.25 days) is primarily attributed to limitations in the analysis method and can be seen as a misfit. This difference may result from factors such as the limited length of the time series (windowing of the data), the presence of colored noise, the resolution of the frequency spectrum, and the difficulty in separating adjacent frequencies. In LODR time series, the annual and semi-annual signals and also signals with periods of 13.66 and 9.13 are significant. It is noteworthy that according to the LS-HE results, tidal effects are still seen in the LODR time series.

5. Prediction of the PM and LOD

In this section, we present a prediction model for the PM and LOD based on the extracted signals in Table 6 using the functional model described in Eq. (14). The Cholesky decomposition was applied to the covariance matrix of the PL noise with a spectral index of $\kappa = -1.5$, allowing us to simulate the observation noise vector for the data. For a comprehensive understanding of this analysis, please refer to the study by (Khazraei and Amiri-Simkooei, 2019).

The prediction process utilized the functional model in conjunction with the observation noise vector to the short, mid, and long-term prediction interval of the PM and LOD time series, spanning from September 1, 2021, to the end of December 2022. This forecast interval was rolled forward weekly, resulting in a total of 70 prediction intervals. The chosen time span was selected to facilitate a fair comparison with the results of the Second EOP PCC. To ensure a fair comparison of this study's results with the EOP PCC, it is important to note that the data from the last day is unavailable for real-time predictions (due to the integration of C04 data with Bulletins). Consequently, we have designated this day as the day zero for our predictions.

In the EOP PCC, each prediction group is assigned a unique identifier (ID) and required to submit weekly forecasts. Table 7 provides further details on the prediction methods used by these groups and the number of submissions. Fig. 4 illustrate the results of our prediction model compared to those from the campaign.

As shown in Fig. 4, the results indicate that the proposed LS-HE + Power Law model demonstrates accuracy comparable to that of other prediction methods. Our model performs particularly well in the initial days of the forecast interval, showcasing its robustness in short-term predictions. This outcome highlights the potential of the LS-HE + Power Law model as a highly effective approach for predicting the PM and LOD time series. In medium-term forecasting, the accuracies for x and y demonstrate strong performance relative to other methods; however, this performance has decreased for LOD. In long-term forecasting, the proposed method continues to exhibit superior performance for both x and y, while the accuracy for LOD has improved significantly.

Table 7
Details of prediction methods and the number of submissions by campaign groups.

ID	Prediction Method	Number of Submissions
100	LS + AR	70
101	LS + AR with piecewise parameter optimization	55
105	LS + AR	68
108	LS + MAR	66
113	LS + AR	43
114	LS	43
115	ANN	43
117	SSA + Copula	58
121	NTFT	67
123	unknown	43
141	LS + Kriging	38
156	LS + ARIMA	31

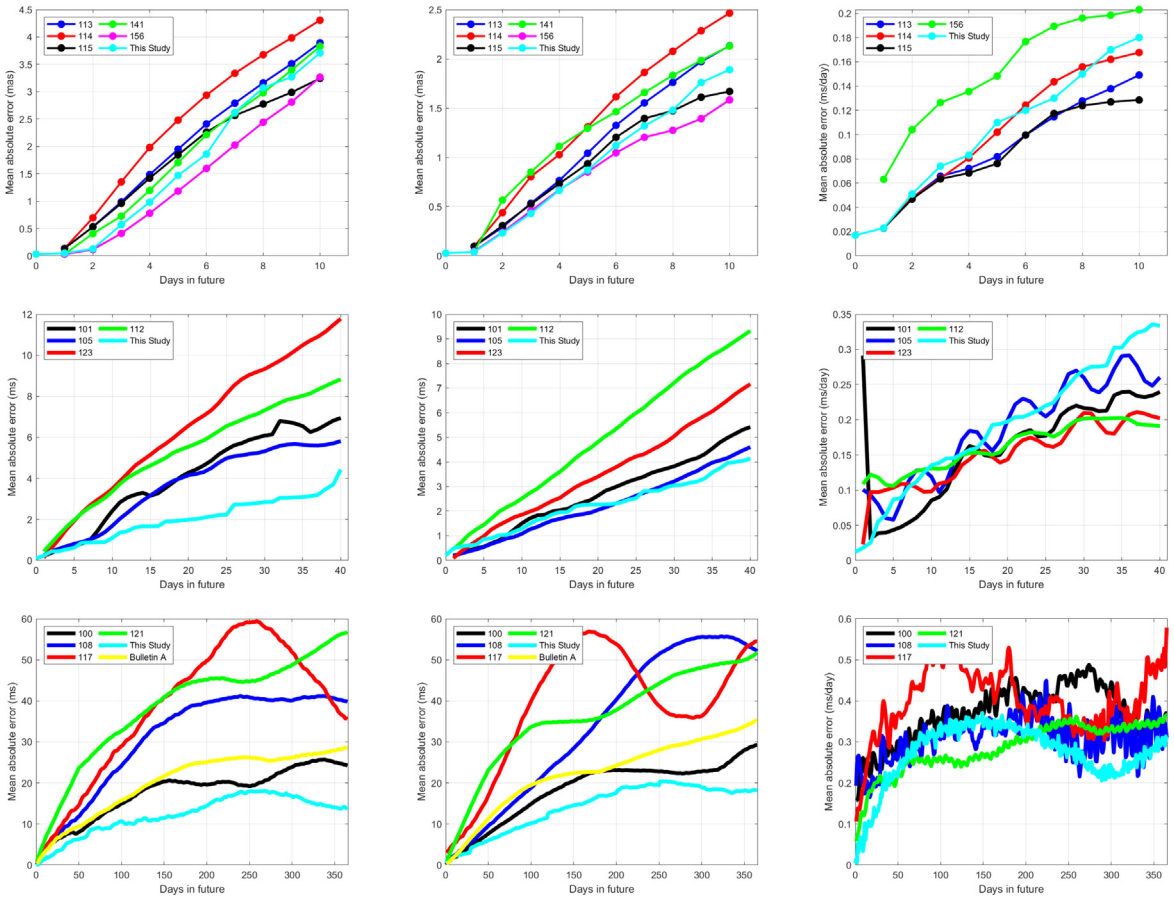

Fig. 4. Results of the proposed prediction method and other methods in EOP PCC in three stages including short, mid, and long term consideration. The first, second, and third columns belong to x, y, and LOD, respectively.

6. Summary and conclusions

This study provides an in-depth analysis of the PM and LOD time series, encompassing both deterministic and stochastic behaviors. This investigation yields critical insights into Earth's internal and external dynamics, supporting a range of geodetic and geophysical applications. Proper identification of the deterministic and stochastic components in the PM and LOD is essential for enhancing prediction accuracy, meeting the high-precision objectives set by the Global Geodetic Observing System (GGOS) of the International Association of Geodesy (IAG), which aims for 1 mm accuracy and 0.1 mm/year stability on global scales in the International Terrestrial Reference Frame (ITRF) defining parameters (Plag and Pearlman, 2009).

In this research, the PM components (x and y) and LOD time series from the IERS EOP 14 C04 data set were examined. The stochastic characteristics of the PM and LOD time series were modeled by a power-law (PL) noise process, with the optimal noise model being a combination of white noise and PL noise with a spectral index of −1.5 for all three time series analyzed. Additionally, effects from solid Earth and ocean tides in the LOD time series were modeled and removed in accordance with the IERS Convention 2010, enhancing the accuracy of further analysis. Periodic patterns within the PM and LOD were extracted using the least squares harmonic estimation (LS-HE) method. The extracted signals were examined for their potential geophysical causes, statistical significance against colored noise, and their amplitude. The most significant signals identified were the 433.61-day (Chandler) and 366.50-day (annual) signals in the PM time series, as well as the annual, semi-annual, 9-day, and 13-day signals in the LOD time series. These signals, contributing notably to the variations in the PM and LOD, were statistically robust even in the presence of underlying colored noise.

Finally, by integrating the LS-HE method with the identified colored noise model, we successfully projected short, mid, and long-term predictions of the PM and LOD time series. Our results indicate that this combined approach is an effective method for short-term prediction of the PM and LOD time series. The mid- and long-term forecasts of PM time series have high accuracy compared to others, but this accuracy is not as high for LOD time series as for PM. However, we providing short-term accuracy that holds promise for future geodetic and geophysical applications. Apart from that, future work will be to explore the propagation of orbital errors caused by using the proposed the PM and LOD prediction algorithm by using different LEO (Low earth orbit), GEO (Geostation-

ary earth orbit) and MEO (medium earth orbit) GPS satellites blocks. This analysis will be crucial to understand the real impact in the final products observed by the space.

Funding

SB were partially supported by Generalitat Valenciana (SEJIGENT/2021/001). SB was also partially supported by the European Union-NextGenerationEU (ZAMBRANO 21–04).

Declaration of Competing Interest

The authors declare that they have no known competing financial interests or personal relationships that could have appeared to influence the work reported in this paper.

References

Agnew, D., 1992. The time-domain behavior of power-law noises. Geophys. Res. Lett. 19, 333–336. https://doi.org/10.1029/91GL02832.

Amiri-Simkooei, A., 2007. Least-squares variance component estimation: theory and GPS applications. Delft University of Technology, Delft.

Amiri-Simkooei, A., 2009. Noise in multivariate gps position time-series. J. Geodesy 83, 175–187. https://doi.org/10.1007/s00190-008-0251-8.

Amiri-Simkooei, A., 2013. On the nature of gps draconitic year periodic pattern in multivariate position time series. J. Geophys. Res.: Solid Earth 118, 2500–2511. https://doi.org/10.1002/jgrb.50199.

Amiri-Simkooei, A., 2016. Non-negative least-squares variance component estimation with application to gps time series. J. Geodesy 90, 451–466. https://doi.org/10.1007/s00190-016-0886-9.

Amiri-Simkooei, A., Asgari, J., 2012. Harmonic analysis of total electron contents time series: methodology and results. GPS Solut. 16, 77–88. https://doi.org/10.1007/s10291-011-0208-x.

Amiri-Simkooei, A., Tiberius, C., Teunissen, P., 2007. Assessment of noise in gps coordinate time series: methodology and results. J. Geophys. Res.: Solid Earth 112. https://doi.org/10.1029/2006JB004913.

Belda, S., Ferrándiz, J.M., Heinkelmann, R., et al., 2018. A new method to improve the prediction of the celestial pole offsets. Scient. Rep. 8 (1), 13861. https://doi.org/10.1038/s41598-018-32082-1.

Bizouard, C., 2020. Geophysical modelling of the polar motion volume 31. Walter de Gruyter GmbH & Co KG. https://doi.org/10.1515/9783110298093.

Bizouard, C., Fernandez, L.I., Zotov, L., 2022. Admittance of the earth rotational response to zonal tide potential. J. Geophys. Res.: Solid Earth 127 (3). https://doi.org/10.1029/2021JB022962, e2021JB022962.

Bizouard, C., Lambert, S., Gattano, C., et al., 2019. The iers eop 14c04 solution for earth orientation parameters consistent with itrf 2014. J. Geodesy 93, 621–633. https://doi.org/10.1007/s00190-018-1186-3.

Bos, M., Fernandes, R., Williams, S., et al., 2008. Fast error analysis of continuous gps observations. J. Geodesy 82, 157–166. https://doi.org/10.1007/s00190-007-0165-x.

Brzeziński, A., Bizouard, C., Petrov, S.D., 2002. Influence of the atmosphere on earth rotation: what new can be learned from the recent atmospheric angular momentum estimates? Surv. Geophys. 23, 33–69. https://doi.org/10.1023/A:1014847319391.

Chao, B., O'Connor, W.P., 1988. Global surface-water-induced seasonal variations in the earth's rotation and gravitational field. Geophys. J. Int. 94 (2), 263–270. https://doi.org/10.1111/j.1365-246X.1988.tb05900.x.

Chen, J., Wilson, C., 2005. Hydrological excitations of polar motion, 1993–2002. Geophys. J. Int. 160, 833–839. https://doi.org/10.1111/j.1365-246X.2005.02522.x.

Dahlen, F., 1971. The excitation of the chandler wobble by earthquakes. Geophys. J. Int. 25 (1–3), 157–206. https://doi.org/10.1111/j.1365-246X.1971.tb02336.x.

Dhar, S., Heinkelmann, R., Belda, S., et al., 2024. Combining evolutionary computation with machine learning technique for improved short-term prediction of ut1-utc and length-of-day. Earth, Planets and Space 76 (1), 111. https://doi.org/10.1186/s40623-024-02055-y.

Dill, R., Dobslaw, H., Thomas, M., 2019. Improved 90-day earth orientation predictions from angular momentum forecasts of atmosphere, ocean, and terrestrial hydrosphere. J. Geodesy 93 (3), 287–295. https://doi.org/10.1007/s00190-018-1158-7.

Freedman, A., Steppe, J., Dickey, J., et al., 1994. The short-term prediction of universal time and length of day using atmospheric angular momentum. J. Geophys. Res.: Solid Earth 99, 6981–6996. https://doi.org/10.1029/93JB02976.

Gross, R., Eubanks, T., Steppe, J., et al., 1998. A kalman-filter-based approach to combining independent earth-orientation series. J. Geodesy 72, 215–235. https://doi.org/10.1007/s001900050162.

Gross, R.S., 2000. The excitation of the chandler wobble. Geophys. Res. Lett. 27 (15), 2329–2332. https://doi.org/10.1029/2000GL011450.

Gross, R.S., Fukumori, I., Menemenlis, D., 2003. Atmospheric and oceanic excitation of the earth's wobbles during 1980–2000. J. Geophys. Res.: Solid Earth 108 (B8). https://doi.org/10.1029/2002JB002143.

Guessoum, S., Belda, S., Ferrandiz, J.M., et al., 2022. The short-term prediction of length of day using 1d convolutional neural networks (1d cnn). Sensors 22 (23), 9517. https://doi.org/10.3390/s22239517.

Guinot, B., Robbins, A., Ashkenazi, V., et al., 1980. Determination of the motion of the pole, and comparison with astrometry. Philos. Trans. Roy. Soc. London Ser. A, Math. Phys. Sci. 294, 329–334. https://doi.org/10.1098/rsta.1980.0039.

Guo, J., Li, Y., Dai, C., et al., 2013. A technique to improve the accuracy of earth orientation prediction algorithms based on least squares extrapolation. J. Geodyn. 70, 36–48. https://doi.org/10.1016/j.jog.2013.06.002.

Hamdan, K., Sung, L.-Y., 1996. Stochastic modeling of length of day and universal time. J. Geodesy 70, 307–320. https://doi.org/10.1007/BF00868182.

Hide, R., 1977. Experiments with rotating fluids. Quart. J. Roy. Meteorol. Soc. 103 (435), 1–28.

Höpfner, J., 2004. Low-frequency variations, chandler and annual wobbles of polar motion as observed over one century. Surv. Geophys. 25, 1–54. https://doi.org/10.1023/B:GEOP.0000015345.88410.36.

Höpfner, J., 1996. Seasonal oscillations in length-of-day. Astron. Nachr. 317, 273–280. https://doi.org/10.1002/asna.2113170406.

Jin, X., Guo, J., Shen, Y., et al., 2021a. Application of singular spectrum analysis and multilayer perceptron in the mid-long-term polar motion prediction. Adv. Space Res. 68 (9), 3562–3573. https://doi.org/10.1016/j.asr.2021.06.039.

Jin, X., Liu, X., Guo, J., et al., 2021b. Analysis and prediction of polar motion using mssa method. Earth, Planets and Space 73, 147. https://doi.org/10.1186/s40623-021-01477-2.

Johnson, T.J., Luzum, B.J., Ray, J.R., 2005. Improved near-term earth rotation predictions using atmospheric angular momentum analysis and forecasts. J. Geodyn. 39 (3), 209–221. https://doi.org/10.1016/j.jog.2004.10.004.

Kalarus, M., Kosek, W., 2004. Prediction of earth orientation parameters by artificial neural networks. Artif. Satellites-J. Planet. Geodesy 39 (2), 175–184.

Kalarus, M., Schuh, H., Kosek, W., et al., 2010. Achievements of the earth orientation parameters prediction comparison campaign. J. Geodesy 84, 587–596. https://doi.org/10.1007/s00190-010-0387-1.

Khazraei, S., Amiri-Simkooei, A., 2019. On the application of monte carlo singular spectrum analysis to gps position time series. J. Geodesy 93, 1401–1418. https://doi.org/10.1007/s00190-019-01253-x.

Kiani Shahvandi, M., Adhikari, S., Dumberry, M., et al., 2024. Contributions of core, mantle and climatological processes to earth's polar motion. Nat. Geosci. 17 (7), 705–710, doi:s41561-024-01478-2.

Kiani Shahvandi, M., Schartner, M., Soja, B., 2022. Neural ode differential learning and its application in polar motion prediction. J. Geophys. Res.: Solid Earth 127 (11). https://doi.org/10.1029/2022JB024775, e2022JB024775.

King, N., Agnew, D.C., 1991. How large is the retrograde annual wobble?. Geophys. Res. Lett. 18 (9), 1735–1738. https://doi.org/10.1029/91GL01882.

Kong, Q., Han, J., Jin, X., et al., 2023. Polar motion prediction using the combination of ssa and arma. Geodesy Geodynam. 14 (4), 368–376. https://doi.org/10.1016/j.geog.2022.12.004.

Kosek, W., Kalarus, M., Niedzielski, T., et al., 2007. Forecasting of the earth orientation parameters: comparison of different algorithms. Citeseer.

Kosek, W., McCarthy, D., Luzum, B., 1998. Possible improvement of earth orientation forecast using autocovariance prediction procedures. J. Geodesy 72, 189–199. https://doi.org/10.1007/s001900050160.

Kuehne, J., Wilson, C.R., 1991. Terrestrial water storage and polar motion. J. Geophys. Res.: Solid Earth 96 (B3), 4337–4345. https://doi.org/10.1029/90JB02573.

Kur, T., Śliwińska-Bronowicz, J., Wińska, M., et al., 2024. Prospects of predicting the polar motion based on the results of the second earth orientation parameters prediction comparison campaign. Earth and Space Science 11 (11). https://doi.org/10.1029/2023EA003278, e2023EA003278.

Lambeck, K., 2005. The Earth's variable rotation: geophysical causes and consequences. Cambridge University Press.

Le Mouël, J., Lopes, F., Courtillot, V., et al., 2019. On forcings of length of day changes: From 9-day to 18.6-year oscillations. Phys. Earth Planet. Inter. 292, 1–11. https://doi.org/10.1016/j.pepi.2019.04.006.

Lenhardt, H., Groten, E., 1985. Chandler wobble parameters from bih and ils data. Manuscr. Geoda. 10 (4), 296–305. https://doi.org/10.1007/BF03655140.

Lichten, S., Marcus, S., Dickey, J., 1992. Sub-daily resolution of earth rotation variations with global positioning system measurements. Geophys. Res. Lett. 19, 537–540. https://doi.org/10.1029/92GL00563.

Malkin, Z., Miller, N., 2010. Chandler wobble: two more large phase jumps revealed. Earth, Planets and Space 62, 943–947. https://doi.org/10.5047/eps.2010.11.002.

Mandelbrot, B., 1982. The fractal geometry of nature. W.H. Freeman, New York.

Mathews, P.M., Herring, T.A., Buffett, B.A., 2002. Modeling of nutation and precession: New nutation series for nonrigid earth and insights into the earth's interior. J. Geophys. Res.: Solid Earth 107 (B4), ETG-3. https://doi.org/10.1029/2001JB000390.

Michalczak, M., Ligas, M., Belda, S. et al., 2024. Advancing polar motion prediction with derivative information. J. Appl. Geodesy, (0).

Modiri, S., Belda, S., Heinkelmann, R., et al., 2018. Polar motion prediction using the combination of ssa and copula-based analysis. Earth, Planets and Space 70, 115. https://doi.org/10.1186/s40623-018-0888-3.

Modiri, S., Belda, S., Hoseini, M., et al., 2020. A new hybrid method to improve the ultra-short-term prediction of lod. J. Geodesy 94, 23. https://doi.org/10.1007/s00190-020-01354-y.

Modiri, S., Thaller, D., Belda, S., et al., 2024. Eop prediction based on multi and single technique space geodetic solution. Int. Assoc. Geodesy Symposia, 1–11. https://doi.org/10.1007/1345_2024_251.

Munk, W., Mohamed Hassan, E.S., 1961. Atmospheric excitation of the earth's wobble. Geophys. J. Int. 4 (Supplement_1), 339–358. https://doi.org/10.1111/j.1365-246X.1961.tb06824.x.

Nastula, J., Gross, R., Salstein, D.A., 2012. Oceanic excitation of polar motion: Identification of specific oceanic areas important for polar motion excitation. J. Geodyn. 62, 16–23. https://doi.org/10.1016/j.jog.2012.01.002.

Niedzielski, T., Kosek, W., 2008. Prediction of ut1–utc, lod and aam $\chi 3$ by combination of least-squares and multivariate stochastic methods. J. Geodesy 82, 83–92. https://doi.org/10.1007/s00190-007-0158-9.

Nikolaidis, R., 2002. Observation of geodetic and seismic deformation with the Global Positioning System Ph.D. thesis. University of California, San Diego.

Petit, G., & Luzum, B., 2010. IERS Conventions (2010). Sèvres, France: Bureau International des Poids et Mesures.

Plag, H.-P., Pearlman, M., 2009. Global Geodetic Observing System: Meeting the Requirements of a Global Society on a Changing Planet in 2020. Springer, Berlin.

Ray, R.D., Erofeeva, S.Y., 2014. Long-period tidal variations in the length of day. J. Geophys. Res.: Solid Earth 119 (2), 1498–1509. https://doi.org/10.1002/2013JB010830.

Rochester, M., Hide, R., Wilkins, G., et al., 1984. Causes of fluctuations in the rotation of the earth. Philos. Trans. Roy. Soc. London Ser. A, Math. Phys. Sci. 313, 95–105. https://doi.org/10.1098/rsta.1984.0086.

Rosen, R., 1993. The axial momentum balance of earth and its fluid envelope. Surv. Geophys. 14, 1–29. https://doi.org/10.1007/BF01044076.

Schuh, H., Schmitz-Hübsch, H., 2000. Short period variations in earth rotation as seen by vlbi. Surv. Geophys. 21, 499–520. https://doi.org/10.1023/A:1006769727728.

Schuh, H., Ulrich, M., Egger, D., et al., 2002. Prediction of earth orientation parameters by artificial neural networks. J. Geodesy 76, 247–258. https://doi.org/10.1007/s00190-001-0242-5.

Shen, W., Peng, C., 2016. Detection of different-time-scale signals in the length of day variation based on eemd analysis technique. Geodesy Geodynam. 7, 180–186. https://doi.org/10.1016/j.geog.2016.05.002.

Shen, Y., Guo, J., Liu, X., et al., 2018. Long-term prediction of polar motion using a combined ssa and arma model. J. Geodesy 92, 333–343. https://doi.org/10.1007/s00190-017-1065-3.

Sliwinska-Bronowicz, J., Kur, T., Winska, M., et al., 2024. Assessment of length-of-day and universal time predictions based on the results of the second earth orientation parameters prediction comparison campaign. J. Geodesy 98 (3), 1–34. https://doi.org/10.1007/s00190-024-01824-7.

Stamatakos, N., 2017. Iers rapid service prediction center products and services: improvement, changes, and challenges, 2012 to 2017. In: In Proceedings of the Journées Systèmes de référence spatio-temporels.

Tapley, B., Schutz, B., Eanes, R., 1985. Station coordinates, baselines, and earth rotation from lageos laser ranging: 1976–1984. J. Geophys. Res.: Solid Earth 90, 9235–9248. https://doi.org/10.1029/JB090iB11p09235.

Teunissen, P., Amiri-Simkooei, A., 2008. Least-squares variance component estimation. J. Geodesy 82 (2), 65–82. https://doi.org/10.1007/s00190-007-0157-x.

Wahr, J., 1988. The earth's rotation. Annu. Rev. Earth Planet. Sci. 16, 231–249. https://doi.org/10.1146/annurev.ea.16.050188.001311.

Wang, C., Zhang, P., 2023. Improving the accuracy of polar motion prediction using a hybrid least squares and long short-term memory model. Earth, Planets and Space 75 (1), 153. https://doi.org/10.1186/s40623-023-01910-8.

Wang, G., Liu, L., Su, X., et al., 2016. Variable chandler and annual wobbles in earth's polar motion during 1900–2015. Surv. Geophys. 37, 1075–1093. https://doi.org/10.1007/s10712-016-9384-0.

Williams, S., 2003. The effect of coloured noise on the uncertainties of rates estimated from geodetic time series. J. Geodesy 76, 483–494. https://doi.org/10.1007/s00190-002-0283-4.

Williams, S., Bock, Y., Fang, P., et al., 2004. Error analysis of continuous gps position time series. J. Geophys. Res.: Solid Earth 109. https://doi.org/10.1029/2003JB002741.

Wilson, C.R., Haubrich, R.A., 1976. Meteorological excitation of the earth's wobble. Geophys. J. Int. 46 (3), 707–743. https://doi.org/10.1111/j.1365-246X.1976.tb01254.x.

Włodzimierz, H., 1990. Polar motion prediction by the least-squares collocation method. Earth Rotation and Coordinate Reference Frames, 10–11. Springer, Edinburgh, Scotland, August, pp. 50–57. https://doi.org/10.1007/978-1-4684-6399-6_7, 1989.

Wu, F., Chang, G., Deng, K., 2021. One-step method for predicting lod parameters based on ls+ar model. J. Spatial Sci. 66, 317–328. https://doi.org/10.1080/14498596.2019.1618401.

Wu, K., Liu, X., Jin, X., et al., 2023. Precise prediction of polar motion using sliding multilayer perceptron method combining singular spectrum analysis and autoregressive moving average model. Earth, Planets and Space 75 (1), 179. https://doi.org/10.1186/s40623-023-01937-x.

Xu, X., Zhou, Y., Liao, X., 2012. Short-term earth orientation parameters predictions by combination of the least-squares, ar model and kalman filter. J. Geodyn. 62, 83–86. https://doi.org/10.1016/j.jog.2011.12.001.

Zhong, M., Naito, I., Kitoh, A., 2003. Atmospheric, hydrological, and ocean current contributions to earth's annual wobble and length-of-day signals based on output from a climate model. J. Geophys. Res.: Solid Earth 108 (B1). https://doi.org/10.1029/2001JB000457.

Zotov, L., Xu, X., Zhou, Y., et al., 2018. Combined sai-shao prediction of earth orientation parameters since 2012 till 2017. Geodesy Geodynam. 9 (6), 485–490. https://doi.org/10.1016/j.geog.2018.11.002.

Iz, H., 2008. Polar motion modeling, analysis, and prediction with time dependent harmonic coefficients. J. Geodesy 82, 871–881. https://doi.org/10.1007/s00190-008-0215-z.